Vertical profiles of aerosol mass concentration derived by unmanned airborne in-situ and remote sensing instruments during dust events.

Dimitra Mamali [1], Eleni Marinou [2,3,4], Jean Sciare [5], Michael Pikridas [5], Panagiotis Kokkalis [2,6], Michael Kottas [2], Ioannis Binietoglou [2,7], Alexandra Tsekeri [2], Christos Keleshis [5], Ronny Engelmann [8], Holger Baars [8], Albert Ansmann [8], Vassilis Amiridis [2], Herman Russchenberg [1], and George Biskos [5,1]

[1]Department of Geoscience and Remote Sensing, Delft University of Technology, Delft, The Netherlands
[2]Institute for Astronomy, Astrophysics, Space Applications and Remote Sensing, National Observatory of Athens, Greece
[3]Department of Physics, Aristotle University of Thessaloniki, Thessaloniki, Greece
[4]Deutsches Zentrum für Luft- und Raumfahrt (DLR), Institut für Physik der Atmosphäre, Oberpfaffenhofen, Germany
[5]The Cyprus Institute, Energy, Environment and Water Research Centre, Nicosia, Cyprus
[6]Physics Department, Faculty of Science, Kuwait University, Kuwait
[7]National Institute for Research and Development in Optoelectronics, Ilfov, Romania
[8]Leibniz Institute for Tropospheric Research, Leipzig, Germany

Correspondence: Dimitra Mamali (D.Mamali@tudelft.nl) and George Biskos (G.Biskos@tudelft.nl; G.Biskos@cyi.ac.cy)

Abstract. In-situ measurements using Unmanned Aerial Vehicles (UAVs) and remote sensing observations can independently provide dense vertically-resolved measurements of atmospheric aerosols; information which is highly required in climate models. In both cases, inverting the recorded signals to useful information requires assumptions and constraints, and this can make the comparison of the results difficult. Here we compare, for the first time, vertical profiles of the aerosol mass concentration derived from Light Detection And Ranging (LIDAR) observations and in-situ measurements using an Optical Particle Counter (OPC) onboard a UAV during moderate and weak Saharan dust episodes. Agreement between the two measurement methods was within experimental uncertainty for the coarse mode (i.e., particles having radii > 0.5 μm) where the properties of dust particles can be assumed with good accuracy. This result proves that the two techniques can be used interchangeably for determining the vertical profiles of the aerosol concentrations, bringing them a step closer towards their systematic exploitation in climate models.

1 Introduction

Aerosol particles affect the atmospheric energy balance directly by interacting with solar radiation, and indirectly through the formation of clouds (Lohmann and Feichter, 2004). Determining the radiative forcing of the atmospheric aerosol particles is highly uncertain partly because of the significant spatial (both vertically and horizontally) and temporal variability of their concentration, size, and chemical composition (IPCC, 2013). The vertical variability in the properties of the atmospheric aerosol can be independently determined by modern in-situ measurements using airborne platforms and remote-sensing observations. Comparison of the measurements obtained by these two types of techniques, however, is fundamental for improving the accu-

racy of the resulting observational data for use in climate models.

Light Detection And Ranging (LIDAR) instruments are among the most powerful tools for probing vertically-resolved properties of the atmospheric aerosol. A number of retrieval algorithms that have been developed over the years can be used to obtain aerosol optical parameters from the LIDAR raw signals, including the aerosol backscatter coefficient β_{aer} (Klett, 1981; Fernald, 1984), the aerosol extinction coefficient α_{aer} (Ansmann et al., 1990, 1992), and the particle depolarization ratio δ^p (Freudenthaler et al., 2009). Under certain assumptions, recently developed algorithms can now be used to retrieve other vertically resolved aerosol properties such as particle absorption and mass concentration using the synergy of LIDAR and sun-photometer (Ansmann et al., 2011; Lopatin et al., 2013; Chaikovsky et al., 2016). To check the validity of these assumptions and to assure the quality of the final data, certain aerosol properties retrieved from LIDAR observations have been compared with vertical in-situ observations using research aircraft (Feingold and Morley, 2003; Weinzierl et al., 2011; Bravo-Aranda et al., 2015; Granados-Muñoz et al., 2016; Rosati et al., 2016; Kokkalis et al., 2017; Tsekeri et al., 2017).

Airborne in-situ measurements using research aircraft are complex and costly, and therefore their availability is scarce and time-restricted, limiting comparability with remote sensing observations. What is more, manned aircraft cannot cover the lowermost part of the atmosphere due to safety restrictions, posing another major limitation. Recent efforts in aerosol instrumentation have provided lightweight and miniaturized instruments that can measure the size and concentration of aerosol particles onboard UAVs (Altstädter et al., 2015; Bezantakos et al., 2015; Barmpounis et al., 2016; Brady et al., 2016; Renard et al., 2016; Surawski et al., 2017; Bezantakos et al., 2017) in a much simpler and cost-effective manner. As a result, vertical profiling of key aerosol parameters can now be performed over long periods of time on a routine basis, and at much lower altitudes compared to measurements with manned research aircraft. Considering, however, that these advantages come in many cases at the expense of the quality of the recorded data, measurements of aerosol properties using miniaturized instruments onboard UAVs need to be validated before using them to bridge the long-lasting gap between in-situ measurements and remote sensing observations.

Here we compare, for the first time to our knowledge, vertical profiles of the aerosol mass concentration, derived from LIDAR measurements using the POlarization LIDAR PHOtometer Networking technique (POLIPHON), and in-situ measurements with an OPC onboard a UAV (hereafter referred to as OPC_a). It should be noted that the two techniques do not measure the mass concentration directly, but this is estimated from the recorded signals of the two instruments. The measurements were recorded during the BACCHUS-INUIT-ACTRIS (Impact of Biogenic Versus Anthropogenic emissions on Clouds and Climate: towards a Holistic UnderStanding; Ice Nuclei Research Unit; European Research Infrastructure for the observation of Aerosol, Clouds and Trace gases Research InfraSctructure network) campaign that took place in Cyprus during April 2016.

2 Instrumentation and Methods

2.1 Site Description

Cyprus is located in the Eastern Mediterranean (cf. Figure 1 inset), receiving air masses from Europe, the Middle East and North Africa (Lelieveld et al., 2002). Therefore, it represents an ideal location for characterizing different aerosol types and

5 investigating the role of particles in various atmospheric processes.

The measurements reported here were conducted at three different locations. Aerial measurements, using a UAV, were carried out at Orounda (35º09′ N; 33º07′ E; 310 m above sea level; a.s.l.), providing highly-resolved spatially and temporally distributed data up to ca. 2 km above ground level (a.g.l.). Ground-based in-situ aerosol measurements, were performed at the

10 Cyprus Atmospheric Observatory (CAO) at Agia Marina-Xyliatou (35º04′ N; 33º06′ E; 535 m a.s.l.), located 6.5 km south of Orounda. A Polly^{XT} Raman LIDAR was located at the suburbs of Nicosia (35º14′ N; 33º38′ E; 190 m a.s.l.), ca. 35 km east of Orounda, providing round-the-clock measurements of the atmospheric conditions up to 12 km a.g.l.. The exact locations of the measuring points are shown in Figure 1 and detailed descriptions of the instruments are given below.

2.2 Unmanned Aerial Vehicle (UAV)

15 The UAV employed during the campaign (cf. Figure 2) has a fixed wingspan of 3.8 m, and is powered by a two-stroke internal combustion engine. It has a take-off weight of 35 kg that results in a payload capacity of approximately 12 kg. The payload bay is 1.3 m × 0.23 m × 0.34 m (length-width-height), and can fit multiple instruments. When loaded, the UAV can fly for up to 4 hours with an air speed velocity of 25 ± 10 m s^{-1} and can reach altitudes up to 4 km a.g.l. (due to airspace limitations, however, only flights up to 2 km were permitted). An autopilot system allowed predetermined flight plans that involved spiral

20 rectangular-shaped ascending and descending patterns (cf. Figure S1 of the Supplementary Material) preventing contamination of the sampling system from the engine's exhaust. For consistency, the results shown in the rest of the paper correspond to measurements during ascends.

2.3 UAV-based Optical Particle Counter Measurements

Vertical profiles of the particle size distributions of the atmospheric aerosol were measured using an OPC (i.e., the OPC$_a$;

25 MetOne, Model 212-2) onboard the UAV, which reported particle size distributions, ranging from 0.15 to 5 μm in radius, in 8 size bins. The sampled aerosol was dried to below 50% relative humidity (RH) by gently heating the sampling tube of OPC$_a$. Assuming spherical shape and constant mass density for the particles, the size distributions were converted into aerosol mass concentrations (see Section 2.4). In addition to OPC$_a$, a single wavelength aethalometer (AethLabs - Model AE51) with a sampling time resolution of 1 second and a flow rate of 0.2 lpm, was onboard the UAV to verify that no contamination of the

30 sampled air by the engine exhaust took place. Each instrument was equipped with an individual sampling inlet that extended 5

cm from the UAV nose to ensure representative sampling.

2.4 Particle Mass Concentration Calculation from the OPC_a Measurements

The mass concentration profiles of the coarse particles were calculated from the size distribution measurements recorded by OPC_a. Before converting the aerosol number concentrations to mass concentrations, the OPC measurements were averaged over 30 s (original time resolution 1 s). This was found to be optimal for suppressing a high frequency noise of the OPC raw data and at the same time maintaining a relatively high spatial resolution of ~ 80 m in the vertical direction. The number concentration (dN) of each size bin was converted to volume concentration according to $dV(r) = dN(r)\frac{4}{3}\pi r^3$, where r is the mean radius of each size bin in the recorded measurements. The volume concentration of particles with radii larger that 0.5 μm were summed and multiplied by ρ_d, yielding the coarse mode mass concentration. The variability in the number size distributions averaged every 30 s propagated an uncertainty of the order of 10% in the estimated volume size distributions and the mass concentrations of the particles (Taylor, 1997) .

2.5 LIDAR Measurements

A depolarization Raman LIDAR Polly^{XT} (Althausen et al., 2009; Engelmann et al., 2016) was used in the measurements reported here. This LIDAR emits laser pulses simultaneously at three wavelengths: 1064, 532 and 355 nm. The laser beam interacts with the atmospheric molecules and particles, and a part of it (backscattered light) is collected by the receiver unit that consists of two telescopes (near-field and far-field). The elastically backscattered signals are used as input to the Fernald-Klett algorithm (Klett, 1981; Fernald, 1984; Böckmann et al., 2004) to retrieve the vertical profile of the particle backscatter coefficient β_{aer}. This method assumes a linear relationship between the aerosol extinction-to-backscatter ratio constant (i.e., the LIDAR ratio S) throughout the entire atmospheric column; a critical assumption that can induce uncertainties up to 20-30% of the retrieved property from statistical and systematic errors (Bösenberg and Brassington, 1997; Comerón et al., 2004; Rocadenbosch et al., 2010).

In addition to the elastically backscattered signal, Polly^{XT} receives the nitrogen Raman-shifted signal at wavelengths 387 and 607 nm, and the water vapor Raman signal at 407 nm wavelength. The Raman technique (Ansmann et al., 1992; Whiteman et al., 1992) utilizes the elastic and inelastic signals to retrieve the particle extinction α_{aer} and scattering β_{aer} profiles independently, without any critical assumptions. The range-resolved aerosol LIDAR ratio can then be directly estimated as the ratio α_{aer}/β_{aer}. In our analysis, we used the Raman technique to retrieve the α_{aer} and β_{aer} profiles during night-time, and the Fernald-Klett method during day-time when the Raman signal is highly affected from the background noise induced by the scattered sunlight. The Polly^{XT} system also provides information on volume depolarization ratio δ^v from which the particle depolarization ratio δ^p can be estimated (Murayama et al., 1999; Sakai et al., 2000; Shimizu et al., 2004; Sugimoto and Lee, 2006; Freudenthaler et al., 2009). This allows discrimination between spherical particles (e.g., water droplets) and

non-spherical particles such as dust.

2.6 Sun/sky Photometer Measurements

A lunar/sun sky photometer of the Aerosol Robotic Network (AERONET; Holben et al. 1998) was collocated with the LIDAR
at Nicosia, whereas an additional sunphotometer was situated at CAO. Both instruments provided measurements of the Aerosol
Optical Thickness (AOT) at seven wavelengths (i.e., 340, 380, 440, 500, 675, 871 and 1020 nm). The AERONET products
include, among others, parameters corresponding to the total atmospheric column such as the Ångström exponent Å (at several
wavelength pairs), the particle volume size distributions in the size range 0.05 to 15 μm (particle radius), the fine- and coarse
mode AOT (τ_f and τ_c, respectively) at 440, 675, 871, 1020 nm (O'Neill et al., 2003) and the fine- and coarse mode volume
concentrations (v_f and v_c, respectively; Dubovik et al., 2000a, 2006). According to Dubovik et al. (2000b) and Dubovik et al.
(2002) the retrieval of the particle volume size distribution was demonstrated to be adequate in practically all situations with
AOT > 0.05, which was also the case for the observations reported here. Cloud screened and quality assured level 2.0 data
products were used in this work. The uncertainties of the AOT were < 0.02 for UV wavelengths and < 0.01 for wavelengths
above 440 nm (Eck et al., 1999).

2.7 Particle Mass Concentration Profiles Derived by the LIDAR Measurements and the POLIPHON Method

The mass concentration profiles from the LIDAR measurements were calculated using the POLIPHON method (Ansmann
et al., 2011) as stated above. In the first step of the method, the contribution of the fine-mode and coarse mode particles to the
total backscatter coefficient (β_t) is calculated based on depolarization measurements (Tesche et al., 2009). Here we assumed
an externally-mixed aerosol consisting of a fine component with low depolarization ($5 \pm 1\%$; Ansmann et al., 2011), and a
coarse component that induces light depolarization of $31 \pm 4\%$ (Freudenthaler et al., 2009), corresponding to dust particles.
The dust-related backscatter coefficient was determined as:

$$\beta_d = \beta_t \frac{(\delta_t - \delta_{nd})(1 + \delta_d)}{(\delta_d - \delta_{nd})(1 + \delta_t)} \quad , \tag{1}$$

where δ_t, δ_{nd} and δ_d are respectively the observed total depolarization ratio, the assumed non-dust depolarization ratio and the
measured depolarization ratio of dust particles. Once β_d was determined, the non-dust backscatter coefficient was calculated
by $\beta_{nd} = \beta_t - \beta_d$. In the calculations presented here we used β and δ^p values corresponding to 532 nm wavelength.

In the second step of the method, the mass concentrations of the fine (non-dust; m$_{nd}$) and coarse (dust; m$_d$) aerosol fractions
are calculated according to (Ansmann et al., 2011):

$$m_d = \rho_d \overline{(v_c/\tau_c)} \beta_d S_d \tag{2}$$

$$m_{nd} = \rho_{nd} \overline{(v_f/\tau_f)} \beta_{nd} S_{nd} \quad , \tag{3}$$

where ρ is the mass density, whereas the product of the backscattering coefficient and the LIDAR ratio $\beta \cdot S$ is the extinction coefficient of the particles, with subscripts d and nd denoting dust (coarse) and non-dust (fine) particles. It should be noted that the factors $\overline{v_c/\tau_c}$ and $\overline{v_f/\tau_f}$ are used to convert the extinction measurements to particle volume concentration for the coarse and the fine faction, respectively. In this work these factors were determined from the daily mean data of the sunphotometer that was collocated with the LIDAR. The volume concentrations v_f and v_c were obtained from the AERONET data, whereas the fine and coarse mode AOTs, τ_f and τ_c, at 532 nm wavelength, were calculated using Å (determined in the 440-675 wavelength range) according to:

$$\tau_{f,c(532)} = \tau_{f,c(440)} \times \left(\frac{440}{532}\right)^{\text{Å}_{f,c(440-675)}} \tag{4}$$

Another assumption we made was that the LIDAR-derived dust and non-dust fractions are identical to the photometer-derived coarse and fine particle fractions. The inflection point of the AERONET data was adopted as the limit between the fine and the coarse mode particles. As a result, the fine mode ranged between 0.05-0.5 μm (particle radius) and the coarse mode between 0.5-15 μm as shown in Figure 3. The calculated values of $\overline{v_f/\tau_f}$ and $\overline{v_c/\tau_c}$ (cf. Table 1) are in line with the conversion factors mentioned by Mamouri and Ansmann (2016, 2017) who performed an extensive analysis of the conversion factors of dust over Cyprus.

Apart from v/τ, the other parameters required for determining the aerosol mass concentration from the LIDAR measurements are ρ, β and S. Regarding ρ, we used a density of 2.6 ± 0.6 g cm^{-3} for the coarse mode particles (corresponding to dust according to Gasteiger et al., 2011). Chemical analysis of filter samples collected during the measurements showed that the dust density assumed here is valid (data not shown). Values for S$_{nd}$ (60 ± 10 sr) were taken from the literature (Mamouri and Ansmann, 2014), and actual measurements were used for S$_d$. S$_d$ measurements were only possible during night-time when the Raman channels were operating. We measured the same S$_d$ values (47 ± 10 sr) for both events analyzed here (cf. Figure S2 in the Supporting Information). All the values of the parameters that are required as input for the calculations are summarized in Table 1 .

2.8 POLIPHON Method - Error Estimation

The uncertainties of β_d and β_{nd} in Eq. (1) were calculated using the Monte-Carlo method (Bevington et al., 1993). For each input parameter, we generated 100 normally distributed random numbers. The values provided in Table 1 were used as the mean parameter and the standard deviation of the normal distributions. Then, 100 β_d and β_{nd} values were calculated for each point in the atmospheric column and from these the mean values and the standard deviations (errors) of β_d and β_{nd} were estimated to be 22% and 28%, respectively. For equations (2) and (3) the uncertainties were calculated analytically using the error propagation law.

3 Results and Discussion

3.1 Homogeneity of Aerosol Properties over the Measurement Sites

Given the proximity (6.5 km) of the ground (at CAO) and the airborne in-situ observations (at Orounda), as well as the absence of any strong pollution sources in the region, the measurements were considered to correspond to the same air parcel in terms of atmospheric composition. The third measurement location (Nicosia) was situated 35 km away from the airfield. As suggested by the comparison of sunphotometer measurements at Nicosia and CAO, however, all locations were affected by the same air masses with minor influence from local emissions that were mostly trapped within the Planetary Boundary Layer (PBL).

Figure 4 shows the AOT_{500} and the $Å_{440-870}$ measured by the sunphotometers in Nicosia and at CAO from 13 to 24 April 2016 when concurrent measurements were performed at the two locations. Overall, the temporal variability of these two parameters observed at Nicosia was very similar with the respective measurements at CAO, exhibiting correlations coefficients of 0.89 and 0.87 for AOT_{500} and $Å_{440-870}$, respectively. This good correlation was further enhanced during the dust event cases (e.g., on 15 April 2016) when the relative contribution of the aerosol fine mode was minimized, supporting that a comparison of aerosol measurements at these locations is meaningful. In terms of absolute values, AOT_{500} was 15-50% higher at Nicosia compared to CAO, even during the cases with the dust events, when coarse particles dominated. These higher values at Nicosia are mainly due to the altitudinal difference between the sites (Nicosia is at an altitude of 190 m whereas CAO at 535 m above sea level) and the contribution of the local aerosol sources to the total aerosol burden. This was further justified by the higher $Å_{440-870}$ measurements at Nicosia which signify the presence of small aerosol particles from anthropogenic sources.

3.2 Comparison of the Mass Concentration Measurements

A total of 6 UAV flights with OPC_a onboard were performed during the entire campaign. However, only 2 fulfilled all the necessary requirements for comparison with the LIDAR observations. Those requirements are that 1) there are simultaneous measurements of LIDAR and OPC_a, 2) there are cloud-free conditions or clouds are above 7-8 km altitude so that the LIDAR retrievals can be made, 3) there is enough dust loading, 4) there is availability of AERONET data, and 5) the airborne in-situ measurements were performed before the full development of the PBL. All these requirements were fulfilled during the measurements on 15 and 22 April 2016, which are analyzed below.

3.2.1 Case Study I: 15 April 2016

The atmospheric situation over South-Eastern Europe on 15 April 2016 was dominated by a high-pressure system resulting in mostly cloud-free conditions over Cyprus. A dust event of moderate intensity was observed, resulting in an average AOT_{500} value of 0.4 over Nisosia and CAO (cf. discussion in Section 3.1 and Figure 4). Figure 5 shows the LIDAR time-height display during that day, with the upper panel showing the range-corrected signal of the 1064-nm channel, which provides information

about the aerosol loading and the presence of clouds, and the lower panel the linear volume depolarization ratio δ^v at 532 nm, which is used to discriminate particles of different shapes that can be indicative of different sources. Throughout the day, high concentrations of aerosol particles were observed even up to ca. 7 km altitude (Figure 5a), with a persistent aerosol layer extending from 2.5 to ca. 7 km. Backtrajectory analysis (cf. Figure 6) corroborated that this layer resulted from a Saharan dust event that originated in Algeria and traveled over Italy, Greece and Turkey before reaching Cyprus. Despite passing over polluted areas, the core of the dust layer remained pure (see analysis below) due to its high elevation (>2 km) throughout the path. The δ^v plot (Figure 5b) also shows the temporal evolution of this dust layer. From 00:00-03:00 UTC the dust extends from 2 to 7 km altitude, but later (until 14:00 UTC) it becomes shallower. From the early morning hours (07:00 UTC) to early afternoon (14:00 UTC) when the boundary layer develops, the dust layer is confined above it, reaching up to 5 km altitude. After the collapse of the boundary layer, the dust layer starts to descend and finally reaches the ground at 18:00 UTC.

The cloud-free and time homogeneous atmospheric scene between 07:00 and 07:50 UTC, which overlapped with the time window of the UAV flight, was selected for calculating the parameters of the atmospheric aerosol using the POLIPHON method. As mentioned earlier, the S_d values used as input in POLIPHON were not measured at the same time window (07:00 and 07:50 UTC), but they were derived from night-time measurements. However, back-trajectory analysis verified that the LIDAR was measuring the same air mass type during these time spans (Fig. 6 and Fig. S3). The LIDAR profiles of β (retrieved with the Fernald-Klett method; Section 2.5) and δ^p, that were used as input in POLIPHON (532 nm only), are shown in Figure 7a-b. The backscatter signal increased gradually from 1 Mm^{-1}sr^{-1} at 1 km (532 nm), reaching a maximum of ca. 2.3 Mm^{-1}sr^{-1} at 3 km where the dust layer core was. The pure dust layer spanned from ca. 2.5 to 3.8 km ($\delta^p \sim 30\pm2\%$) while below 2 km, the dust was mixed with almost spherical particles, probably from the residual layer, as indicated by the relatively low δ^p values ranging between 12% and 30%. Figure 7c shows the POLIPHON-derived dust and non-dust related backscatter coefficients β_d and β_{nd} from Equation (1), and respective uncertainties determined by Monte-Carlo calculations (cf. Section 2.8). The backscatter coefficient of the fine-mode particles β_{nd} decreased with altitude, while the dust particles were present even down to 0.7 km. As discussed in 2.5, the LIDAR ratio value used in the Fernald-Klett retrieval and the LIDAR ratio corresponding to the dust particles S_d that is required as input in the POLIPHON algorithm, were estimated from Raman LIDAR measurements performed between 00:00-01:40 UTC (UTC+3 local time), just before sunrise. It should be noted here that Raman measurements are only possible at night as during the day scattered sunlight induces high background noise signal. The fact that the dust layer observed during the Raman measurements had the same origin and followed the same atmospheric path before reaching the measurement site between 07:00-07:50 UTC was confirmed by back-trajectory analysis (Fig. 6 and Fig. S3).

Vertical profiles of the RH measured with the UAV and predicted by the WRF−ARW atmospheric model (Skamarock and Klemp, 2008) showed that the atmosphere was dry enough (RH $\lesssim$ 50%) at the ground level and up to 4 km altitude (Figure 7d). As a result we could safely assume that the aerosol particles were dry and thus changes in the mass density and backscatter coefficient due to water uptake were negligible.

3.2.2 Case Study II: 22 April 2016

Contrary to Case Study I, a low intensity dust event ($AOT_{500} = 0.1$) was recorded over Cyprus on 22 April 2016. The evolution of the boundary layer dominating the atmospheric situation that day is depicted in the LIDAR time-height plots shown in Figure 8. From 00:00 to 10:00 UTC a sparse dust layer extended between 1 and 2 km a.g.l. while after the PBL decay a shallower
5 dust plume was observed between 1 and 1.5 km altitude. According to the back-trajectory analysis (Figure 9) the dust air mass at 1.5 km originated from Egypt at the ground level, then it was elevated and passed over Libya, the Mediterranean and Turkey before reaching Cyprus.

    The UAV flight on that day was performed between 04:22 and 05:16 UTC. The atmospheric scene between 04:20-05:00 UTC
10 (Figure 8) was selected for the comparison due to its stable conditions above 0.8 km. Also in this case, the same procedure as in case I was followed to retrieve the LIDAR profiles that were used as input in the POLIPHON algorithm. The backscatter coefficient, the particle depolarization ratio, the POLIPHON-derived dust and non-dust related backscatter coefficients as well as the RH profiles of this atmospheric scene are shown in Figure 10. In contrast to the estimated δ^p values determined from the measurements on 15 April, here δ^p_{532} decreases gradually with height from 0.8 to 2 km having values between 10-17%. These
15 relatively low δ^p_{532} values indicate a mixture of Saharan dust with spherical continental/pollution particles. This is supported by the paths that the air mass follow between 1-2 km which originated from north-eastern Africa close to Cairo and Alexandria. The LIDAR ratio of 40 ± 7 Sr, measured during the previous night (at a height where the signal is mostly free of noise; i.e. 1.2-1.4 km), agrees with the findings of Schuster et al. (2012) and Nisantzi et al. (2015) who reported respectively that $S_{532} = 40 \pm 5$ Sr and $S_{532} = 47$ Sr for dust originating from eastern Sahara.

20 ### 3.2.3 Particle Mass Concentration Profiles

Figures 11a and 11c shows the mass concentration profiles for the coarse particles (particles larger than 0.5 μm in radius) as derived by the LIDAR observations using POLIPHON method for inversion, and the OPC_a measurements. The LIDAR profiles, were calculated by Equations (2) and (3) using the measured β_d and β_{nd}, profiles and the dust density values from the literature (cf. Table 1). The respective OPC_a profiles were determined by the recorded particle number size distributions
25 assuming the same dust particle density (cf. Section 2.4 for details). To ensure that the LIDAR observations are representative of the atmospheric aerosol over Orounda and over CAO we compare the data for altitudes higher than 0.8 km a.s.l. during morning hours when the PBL was shallow.

    The mass concentration profiles from the LIDAR and the OPC_a observed on 15 April 2016 (Figure 11a), show a good
30 correlation, with R = 0.9. In terms of absolute values, the mass concentrations measured by the OPC_a (red curve) lie within the uncertainty limits (38%) of the LIDAR observations, with the former being equal or lower for the entire range of altitudes, exhibiting a bias ranging from -23.0 to -2.4 μg m^{-3} with a mean of -12.0 μg m^{-3} (Figure 11b). The discrepancies between the two methods can be partly attributed to the assumptions used in POLIPHON: 1) constant S throughout the atmospheric col-

umn, 2) contribution in the coarse mode only from depolarizing particles, and 3) the assumption of an externally-mixed aerosol. Assumptions used for the manipulation of the OPC measurements that can explain differences between the two methods are mainly related to the refractive index and the shape of the particles. The refractive index can notably influence the size distribution measured by the OPC, inducing sizing uncertainties of up to 30% (Rosenberg et al., 2012; Granados-Muñoz et al., 2016).

5   The refractive index used for calibrating OPC_a, however, has a value of for n = 1.59, which is very close to literature values for Saharan dust (n = 1.56; Petzold et al., 2009). The difference between the refractive index values used for the calibration of OPC_a and that used for the retrieval of the LIDAR measurements is estimated to introduce a bias of 2% to the calculated mass concentration values. Regarding particle shape, the effect of non-sphericity the particle sizing by light-scattering instruments having similar scattering angle range that of OPC_a ($90° \pm 60°$) is within less than 20%, with a tendency towards undersizing

10   (Osborne et al., 2008).

Another source of discrepancy between the mass concentrations determined by OPC_a and the LIDAR is the limitation of the former to measure particles larger than a few tens of microns due to aerodynamic inlet loses (sedimentation and inertial deposition), resulting in an underestimation of 20% of the coarse mode volume concentration (cf. yellow-green hatched area

15   in Figure 3). To account for that, we corrected the OPC_a measurements using the formula: $m_{\mathrm{OPC}} = m_{\mathrm{POLIPHON}} \frac{\int_{\mathrm{OPC}_a} dV/d\ln r}{\int_{\mathrm{POLIPHON}} dV/d\ln r}$. This correction significantly improved the agreement between the OPC_a (green curve in Figure 11a) and the LIDAR measurements, constraining the bias range to -11.1 and 8.8 $\mu g\ m^{-3}$ which results in a decreased mean bias of $-1.1\ \mu g\ m^{-3}$. Further statistical analysis between the LIDAR and the corrected OPC_a measurements showed that our hypothesis that the two observations refer to the same aerosol population is valid. To be more specific, the two-tailed T-test yielded a P-value of 0.70

20   (assuming equal variances), indicating that the differences between the mean values of the two types of observations are not statistically significant.

The mass concentration profiles determined by the LIDAR and the OPC_a measurements on 22 April 2016 (Figure 11c) also show a good correlation, with R = 0.9. In terms of absolute values, the mass concentrations determined by the OPC_a mea-

25   surements (green line) are lower compared to those determined by the LIDAR observations for the entire range of altitudes, exhibiting biases in the range from -14.7 to 0.6 $\mu g\ m^{-3}$ with a mean value of $-8.7\ \mu g\ m^{-3}$ (Figure 11d). The integrated volume size distribution measured by the sunphotometer in Nicosia (cf. Figure S4) showed that in this case the OPC_a underestimates the coarse volume fraction by 48%. Upon correction, the mean bias decreases to $-1.6\ \mu g\ m^{-3}$ and, with the exception of one point at 1.8 km altitude, the mass concentration values from the OPC_a lie within the calculated uncertainty resulting

30   from the POLIPHON algorithm used to invert the LIDAR data (32%). At higher altitudes the mass concentration decreases drastically and OPC_a measurements drop below the POLIPHON uncertainty limits. Also in this case, the two-tailed T-test (assuming equal variances) yielded a P-value of 0.05 indicating marginal statistically insignificant differences between the means of the two types of measurements

Overall, the airborne in-situ and LIDAR observations are in good agreement both during the observation of a dense as well as of a weak dust event, after the necessary corrections for the OPC_a measurements. In the case of the moderate dust event the volume concentration fraction that is not captured by the OPC range is small and so is the corresponding correction. In contrast, during the weak dust event, the OPC misses almost 50% of the volume size distribution which introduces large measurement
5   ambiguities.

4   Summary and Conclusions

In this study we compare, for the first time to our knowledge, vertical profiles of the aerosol mass concentrations determined independently by an OPC onboard a UAV and by remote sensing observations using data from a LIDAR and a sunpohotometer. The measurements were performed during two cases of dust events that occurred in the region of the Eastern Mediterranean on
10   15 and 22 April 2016. During those days, the UAV flew up to ca. 2 km altitude with the OPC measuring the size distributions of sampled aerosol particles having radii in the range 0.15-5 μm, from which the aerosol mass concentration was calculated. The same information was retrieved by the concurrent LIDAR and sunphotometer measurements that were inverted using the POLIPHON method.

15   During the measurements on 15 April 2016 the dense dust layer extended from 2 to 4 km, while a mixture of dust and almost spherical particles was observed below 2 km. The mass concentration of the coarse mode particles increased from 30 μg m^{-3}, at ca. 0.8 km, to ca. 70 μg m^{-3}, at ca. 1.8 km. Agreement between the in-situ measurements and the LIDAR observations retrieved with the POLIPHON method was very good (R = 0.9), with the in-situ measurements lying within the POLIPHON uncertainty limits (38%), exhibiting a mean bias of -12.0 μg m^{-3} that can be mainly attributed to the difference in the cut-off
20   diameters measured by the two techniques. Corrections applied to account for this difference in the cut-off diameters further enhanced the agreement, decreasing the mean bias to -1.1 μg m^{-3}.

In the measurements carried out on 22 April 2016, a sparse dust layer was observed between 0.8-2 km altitude during the morning hours. Information from the LIDAR measurements and the backtrajectory analysis suggests that this layer was
25   a mixture of desert dust with continental/pollution particles. Despite that, however, agreement between the airborne in-situ and remote sensing measurements in this case was also very good (R = 0.9). In terms of absolute values, the corrected mass concentrations measured by the airborne OPC were equal or lower than those derived from the LIDAR measurements for the entire range of altitudes and exhibited a mean bias of -1.6 μg m^{-3}. The concentrations measured by the airborne OPC were within the calculated uncertainty of POLIPHON.

30

The measurements reported here indicate that unmanned airborne OPC measurements and LIDAR observations can provide reliable ways to determine coarse mode aerosol mass concentration profiles in the atmospheric column, thereby bridging the

gap between in-situ and remote sensing observations. Considering that both methods can provide dense datasets in a cost-effective manner and on a regular basis, this finding paves the way towards their systematic exploitation in climate models.

Author contributions statement

J.S., A.A. conceived the experiment, E.M., M.P., M.K., C.K., R.E. conducted the experiment(s), D.M. analysed the data, prepared the figures and wrote the manuscript. H.B. applied corrections to LIDAR profiles. G.B. supervised the work and contributed to the writing of the manuscript. P.K., I.B., A.T., E.M. and V.A. supported the data analysis procedure. All authors reviewed the manuscript.

Data availability. The sun photometer datasets used in this study are available at https://aeronet.gsfc.nasa.gov
The OPC datasets analysed during the current study are available from the co-author M.Pikridas (m.pikridas@cyi.ac.cy) on reasonable request.
The Polly^{XT} LIDAR (http://polly.tropos.de) datasets analysed during the current study are available from the co-authors A. Ansmann (albert@tropos.de) and E.Marinou (elmarinou@noa.gr).

Competing interests. The authors declare no competing interests.

Acknowledgements. This project received funding from the European Union's Seventh Framework Program (FP7) project BACCHUS (Impact of Biogenic versus Anthropogenic emissions on Clouds and Climate: towards a Holistic UnderStanding) under grant agreement no. 603445, and the European Union's Horizon 2020 research and innovation program ACTRIS-2 (Aerosols, Clouds and Trace gases Research InfraStructure Network) under grant agreement No 654109.
The authors extend special thanks to Dr. Robin Lewis Modini from the Paul Scherrer Institute for assisting in the Mie Calculations.
PK acknowledges the funding of the Greek State Scholarship Foundation: IKY. Part of this project is implemented within the framework of the Action "Reinforcement of Postdoctoral Researchers" of the Operational Program "Human Resource Development, Education and Lifelong Learning", and is co-financed by the European Social Fund (ESF) and the Greek State (NSRF, 2014-2020).

References

Althausen, D., Engelmann, R., Baars, H., Heese, B., Ansmann, A., Müller, D., and Komppula, M.: Portable Raman lidar PollyXT for automated profiling of aerosol backscatter, extinction, and depolarization, Journal of Atmospheric and Oceanic Technology, 26, 2366–2378, https://doi.org/10.1175/2009JTECHA1304.1, 2009.

5   Altstädter, B., Platis, A., Wehner, B., Scholtz, A., Wildmann, N., Hermann, M., Käthner, R., Baars, H., Bange, J., and Lampert, A.: ALADINA-an unmanned research aircraft for observing vertical and horizontal distributions of ultrafine particles within the atmospheric boundary layer, Atmospheric Measurement Techniques, 8, 1627, https://doi.org/10.5194/amt-8-1627-2015, 2015.

Ansmann, A., Riebesell, M., and Weitkamp, C.: Measurement of atmospheric aerosol extinction profiles with a Raman lidar, Optics letters, 15, 746–748, https://doi.org/10.1364/OL.15.000746, 1990.

10   Ansmann, A., Wandinger, U., Riebesell, M., Weitkamp, C., and Michaelis, W.: Independent measurement of extinction and backscatter profiles in cirrus clouds by using a combined Raman elastic-backscatter lidar, Applied Optics, 31, 7113–7131, https://doi.org/10.1364/AO.31.007113, 1992.

Ansmann, A., Tesche, M., Seifert, P., Gross, S., Freudenthaler, V., Apituley, A., Wilson, K., Serikov, I., Linné, H., Heinold, B., et al.: Ash and fine-mode particle mass profiles from EARLINET-AERONET observations over central Europe after the eruptions of the Eyjafjallajökull

15   volcano in 2010, Journal of Geophysical Research: Atmospheres, 116, https://doi.org/10.1029/2010JD015567, 2011.

Barmpounis, K., Maisser, A., Schmidt-Ott, A., and Biskos, G.: Lightweight differential mobility analyzers: Toward new and inexpensive manufacturing methods, Aerosol Science and Technology, 50, 2–5, 2016.

Bevington, P. R., Robinson, D. K., Blair, J. M., Mallinckrodt, A. J., McKay, S., et al.: Data reduction and error analysis for the physical sciences, Computers in Physics, 7, 415–416, 1993.

20   Bezantakos, S., Huang, L., Barmpounis, K., Attoui, M., Schmidt-Ott, A., and Biskos, G.: A cost-effective electrostatic precipitator for aerosol nanoparticle segregation, Aerosol Science and Technology, 49, iv–vi, https://doi.org/10.1080/02786826.2014.1002829, 2015.

Bezantakos, S., Schmidt-Ott, F., and Biskos, G.: Performance evaluation of the cost-effective and lightweight Alphasense optical particle counter for use onboard unmanned aerial vehicles, Aerosol Science and Technology, pp. 1–8, https://doi.org/10.1080/02786826.2017.1412394, 2017.

25   Böckmann, C., Wandinger, U., Ansmann, A., Bösenberg, J., Amiridis, V., Boselli, A., Delaval, A., De Tomasi, F., Frioud, M., Grigorov, I. V., et al.: Aerosol lidar intercomparison in the framework of the EARLINET project. 2. Aerosol backscatter algorithms, Applied Optics, 43, 977–989, https://doi.org/10.1364/AO.43.005370, 2004.

Bösenberg, J. and Brassington, D. J.: Instrument development for atmospheric research and monitoring: lidar profiling, DOAS and tunable diode laser spectroscopy, vol. 8, Springer Science & Business Media, 1997.

30   Brady, J. M., Stokes, M. D., Bonnardel, J., and Bertram, T. H.: Characterization of a quadrotor unmanned aircraft system for aerosol-particle-concentration measurements, Environmental science & technology, 50, 1376–1383, https://doi.org/10.1021/acs.est.5b05320, 2016.

Bravo-Aranda, J. A., Titos, G., Granados-Muñoz, M. J., Guerrero-Rascado, J. L., Navas-Guzmán, F., Valenzuela, A., Lyamani, H., Olmo, F. J., Andrey, J., and Alados-Arboledas, L.: Study of mineral dust entrainment in the planetary boundary layer by lidar depolarization technique, Tellus B, 67, https://doi.org/10.3402/tellusb.v67.26180, 2015.

35   Chaikovsky, A., Dubovik, O., Holben, B., Bril, A., Goloub, P., Tanré, D., Pappalardo, G., Wandinger, U., Chaikovskaya, L., Denisov, S., et al.: Lidar-Radiometer Inversion Code (LIRIC) for the retrieval of vertical aerosol properties from com-

bined lidar/radiometer data: development and distribution in EARLINET, Atmospheric Measurement Techniques, 9, 1181–1205, https://doi.org/10.1080/02786826.2015.1130216, 2016.

Comerón, A., Rocadenbosch, F., López, M. A., Rodríguez, A., noz, C. M., García-Vizcaíno, D., and Sicard, M.: Effects of noise on lidar data inversion with the backward algorithm, Appl. Opt., 43, 2572–2577, https://doi.org/10.1364/AO.43.002572, 2004.

5   Dubovik, O., King, M. D., et al.: A flexible inversion algorithm for retrieval of aerosol optical properties from Sun and sky radiance measurements, Journal of Geophysical Research, 105, 20 673–20 696, https://doi.org/10.1029/2000JD900282, 2000a.

Dubovik, O., Smirnov, A., Holben, B., King, M., Kaufman, Y., Eck, T., and Slutsker, I.: Accuracy assessments of aerosol optical properties retrieved from Aerosol Robotic Network (AERONET) Sun and sky radiance measurements, Journal of Geophysical Research: Atmospheres, 105, 9791–9806, https://doi.org/10.1029/2000JD900040, 2000b.

10   Dubovik, O., Holben, B., Eck, T. F., Smirnov, A., Kaufman, Y. J., King, M. D., Tanré, D., and Slutsker, I.: Variability of absorption and optical properties of key aerosol types observed in worldwide locations, Journal of the atmospheric sciences, 59, 590–608, https://doi.org/10.1175/1520-0469(2002)059<0590:VOAAOP>2.0.CO;2, 2002.

Dubovik, O., Sinyuk, A., Lapyonok, T., Holben, B. N., Mishchenko, M., Yang, P., Eck, T. F., Volten, H., Munoz, O., Veihelmann, B., et al.: Application of spheroid models to account for aerosol particle nonsphericity in remote sensing of desert dust, Journal of Geophysical

15   Research: Atmospheres, 111, https://doi.org/10.1029/2005JD006619, 2006.

Eck, T., Holben, B., Reid, J., Dubovik, O., Smirnov, A., O'neill, N., Slutsker, I., and Kinne, S.: Wavelength dependence of the optical depth of biomass burning, urban, and desert dust aerosols, Journal of Geophysical Research: Atmospheres, 104, 31 333–31 349, https://doi.org/10.1029/1999JD900923, 1999.

Engelmann, R., Kanitz, T., Baars, H., Heese, B., Althausen, D., Skupin, A., Wandinger, U., Komppula, M., Stachlewska, I. S., Amiridis, V.,

20   Marinou, E., Mattis, I., Linné, H., and Ansmann, A.: The automated multiwavelength Raman polarization and water-vapor lidar Polly[XT]: the neXT generation, Atmospheric Measurement Techniques, 9, 1767–1784, https://doi.org/10.5194/amt-9-1767-2016, 2016.

Feingold, G. and Morley, B.: Aerosol hygroscopic properties as measured by lidar and comparison with in situ measurements, Journal of Geophysical Research: Atmospheres, 108, https://doi.org/10.1029/2002JD002842, 2003.

Fernald, F. G.: Analysis of atmospheric lidar observations- Some comments, Applied optics, 23, 652–653, 1984.

25   Freudenthaler, V., Esselborn, M., Wiegner, M., Heese, B., Tesche, M., Ansmann, A., Müller, D., Althausen, D., Wirth, M., Fix, A., et al.: Depolarization ratio profiling at several wavelengths in pure Saharan dust during SAMUM 2006, Tellus B, 61, 165–179, https://doi.org/10.1111/j.1600-0889.2008.00396.x, 2009.

Gasteiger, J., Groß, S., Freudenthaler, V., and Wiegner, M.: Volcanic ash from Iceland over Munich: mass concentration retrieved from ground-based remote sensing measurements, Atmospheric Chemistry and Physics, 11, 2209–2223, https://doi.org/10.5194/acp-11-2209-

30   2011, 2011.

Granados-Muñoz, M. J., Bravo-Aranda, J. A., Baumgardner, D., Guerrero-Rascado, J. L., Pérez-Ramírez, D., Navas-Guzmán, F., Veselovskii, I., Lyamani, H., Valenzuela, A., Olmo, F. J., et al.: A comparative study of aerosol microphysical properties retrieved from ground-based remote sensing and aircraft in situ measurements during a Saharan dust event, Atmospheric Measurement Techniques, 9, 1113–1133, https://doi.org/10.5194/amt-9-1113-2016, 2016.

35   Hess, M., Koepke, P., and Schult, I.: Optical properties of aerosols and clouds: The software package OPAC, Bulletin of the American meteorological society, 79, 831–844, https://doi.org/10.1175/1520-0477(1998)079<0831:OPOAAC>2.0.CO;2, 1998.

Holben, B. N., Eck, T., Slutsker, I., Tanre, D., Buis, J., Setzer, A., Vermote, E., Reagan, J., Kaufman, Y., Nakajima, T., et al.: AERONET—A federated instrument network and data archive for aerosol characterization, Remote sensing of environment, 66, 1–16, https://doi.org/10.1016/S0034-4257(98)00031-5, 1998.

IPCC, I. C.: The physical science basis. Contribution of working group I to the fifth assessment report of the intergovernmental panel on climate change, 2013.

Klett, J. D.: Stable analytical inversion solution for processing lidar returns, Applied Optics, 20, 211–220, https://doi.org/10.1364/AO.20.000211, 1981.

Kokkalis, P., Amiridis, V., Allan, J. D., Papayannis, A., Solomos, S., Binietoglou, I., Bougiatioti, A., Tsekeri, A., Nenes, A., Rosenberg, P. D., et al.: Validation of LIRIC aerosol concentration retrievals using airborne measurements during a biomass burning episode over Athens, Atmospheric Research, 183, 255–267, https://doi.org/http://dx.doi.org/10.1016/j.atmosres.2016.09.007, 2017.

Lelieveld, J., Berresheim, H., Borrmann, S., Crutzen, P., Dentener, F., Fischer, H., Feichter, J., Flatau, P., Heland, J., Holzinger, R., et al.: Global air pollution crossroads over the Mediterranean, Science, 298, 794–799, https://doi.org/10.1126/science.1075457, 2002.

Lohmann, U. and Feichter, J.: Global indirect aerosol effects: a review, Atmospheric Chemistry and Physics Discussions, 4, 7561–7614, https://doi.org/10.5194/acp-5-715-2005, 2005, 2004.

Lopatin, A., Dubovik, O., Chaikovsky, A., Goloub, P., Lapyonok, T., Tanré, D., and Litvinov, P.: Enhancement of aerosol characterization using synergy of lidar and sun-photometer coincident observations: the GARRLiC algorithm, Atmospheric Measurement Techniques, 6, 2065–2088, 2013.

Mamouri, R. E. and Ansmann, A.: Fine and coarse dust separation with polarization lidar, Atmospheric Measurement Techniques, 7, 3717–3735, https://doi.org/10.5194/amt-7-3717-2014, 2014.

Mamouri, R.-E. and Ansmann, A.: Potential of polarization lidar to provide profiles of CCN-and INP-relevant aerosol parameters, Atmospheric Chemistry and Physics, 16, 5905–5931, https://doi.org/10.5194/acp-16-5905-2016, 2016.

Mamouri, R.-E. and Ansmann, A.: Potential of polarization/Raman lidar to separate fine dust, coarse dust, maritime, and anthropogenic aerosol profiles, Atmospheric Measurement Techniques, 10, 3403, https://doi.org/10.5194/amt-10-3403-2017, 2017.

Murayama, T., Okamoto, H., Kaneyasu, N., Kamataki, H., and Miura, K.: Application of lidar depolarization measurement in the atmospheric boundary layer: Effects of dust and sea-salt particles, Journal of Geophysical Research: Atmospheres, 104, 31781–31792, https://doi.org/10.1029/1999JD900503, 1999.

Nisantzi, A., Mamouri, R.-E., Ansmann, A., Schuster, G., and Hadjimitsis, D. G.: Middle East versus Saharan dust extinction-to-backscatter ratios, Atmospheric Chemistry and Physics, 15, 7071–7084, https://doi.org/10.5194/acp-15-7071-2015, 2015.

O'Neill, N., Eck, T., Smirnov, A., Holben, B., and Thulasiraman, S.: Spectral discrimination of coarse and fine mode optical depth, Journal of Geophysical Research: Atmospheres, 108, https://doi.org/10.1029/2002JD002975, 2003.

Osborne, S. R., Johnson, B. T., Haywood, J. M., Baran, A. J., Harrison, M. A. J., and McConnell, C. L.: Physical and optical properties of mineral dust aerosol during the Dust and Biomass-burning Experiment, Journal of Geophysical Research: Atmospheres, 113, n/a–n/a, https://doi.org/10.1029/2007JD009551, http://dx.doi.org/10.1029/2007JD009551, d00C03, 2008.

Petzold, A., Rasp, K., Weinzierl, B., Esselborn, M., Hamburger, T., Dörnbrack, A., Kandler, K., Schütz, L., Knippertz, P., Fiebig, M., et al.: Saharan dust absorption and refractive index from aircraft-based observations during SAMUM 2006, Tellus B, 61, 118–130, https://doi.org/10.1111/j.1600-0889.2008.00383.x, 2009.

Renard, J.-B., Dulac, F., Berthet, G., Lurton, T., Vignelles, D., Jégou, F., Tonnelier, T., Jeannot, M., Couté, B., Akiki, R., et al.: LOAC: a small aerosol optical counter/sizer for ground-based and balloon measurements of the size distribution and nature of atmospheric

particles–Part 2: First results from balloon and unmanned aerial vehicle flights, Atmospheric Measurement Techniques, 9, 3673–3686, https://doi.org/10.5194/amt-9-1721-2016, 2016.

Rocadenbosch, F., Reba, M. N. M., Sicard, M., and Comerón, A.: Practical analytical backscatter error bars for elastic one-component lidar inversion algorithm, Applied optics, 49, 3380–3393, https://doi.org/10.1364/AO.49.003380, 2010.

5 Rolph, G.: Real-time Environmental Applications and Display sYstem (READY), NOAA Air Resources Laboratory, Silver Spring, MD, Website (http://www. arl. noaa. gov/ready/hysplit4. html), 2003.

Rosati, B., Herrmann, E., Bucci, S., Fierli, F., Cairo, F., Gysel, M., Tillmann, R., Größ, J., Gobbi, G. P., Di Liberto, L., et al.: Studying the vertical aerosol extinction coefficient by comparing in situ airborne data and elastic backscatter lidar, Atmospheric Chemistry and Physics, 16, 4539–4554, https://doi.org/10.5194/acp-16-4539-2016, 2016.

10 Rosenberg, P., Dean, A., Williams, P., Dorsey, J., Minikin, A., Pickering, M., and Petzold, A.: Particle sizing calibration with refractive index correction for light scattering optical particle counters and impacts upon PCASP and CDP data collected during the Fennec campaign, Atmospheric Measurement Techniques, 5, 1147–1163, https://doi.org/10.5194/amt-5-1147-2012, 2012.

Sakai, T., Shibata, T., Kwon, S.-A., Kim, Y.-S., Tamura, K., and Iwasaka, Y.: Free tropospheric aerosol backscatter, depolarization ratio, and relative humidity measured with the Raman lidar at Nagoya in 1994–1997: contributions of aerosols from the Asian Continent and the
15 Pacific Ocean, Atmospheric Environment, 34, 431–442, https://doi.org/10.1016/S1352-2310(99)00328-3, 2000.

Schuster, G. L., Vaughan, M., MacDonnell, D., Su, W., Winker, D., Dubovik, O., Lapyonok, T., and Trepte, C.: Comparison of CALIPSO aerosol optical depth retrievals to AERONET measurements, and a climatology for the lidar ratio of dust, Atmospheric Chemistry and Physics, 12, 7431, https://doi.org/10.5194/acp-12-7431-2012, 2012.

Shimizu, A., Sugimoto, N., Matsui, I., Arao, K., Uno, I., Murayama, T., Kagawa, N., Aoki, K., Uchiyama, A., and Yamazaki, A.: Continuous
20 observations of Asian dust and other aerosols by polarization lidars in China and Japan during ACE-Asia, Journal of Geophysical Research: Atmospheres, 109, https://doi.org/10.1029/2002JD003253, 2004.

Skamarock, W. C. and Klemp, J. B.: A time-split nonhydrostatic atmospheric model for weather research and forecasting applications, Journal of Computational Physics, 227, 3465–3485, https://doi.org/10.1016/j.jcp.2007.01.037, 2008.

Stein, A., Draxler, R. R., Rolph, G. D., Stunder, B. J., Cohen, M., and Ngan, F.: NOAA's HYSPLIT atmospheric transport and dispersion
25 modeling system, Bulletin of the American Meteorological Society, 96, 2059–2077, https://doi.org/10.1175/BAMS-D-14-00110.1, 2015.

Sugimoto, N. and Lee, C. H.: Characteristics of dust aerosols inferred from lidar depolarization measurements at two wavelengths, Applied optics, 45, 7468–7474, https://doi.org/10.1364/AO.45.007468, 2006.

Surawski, N., Bezantakos, S., Barmpounis, K., Dallaston, M., Schmidt-Ott, A., and Biskos, G.: A tunable high-pass filter for simple and inexpensive size-segregation of sub-10-nm nanoparticles, Scientific Reports, 7, 45 678, https://doi.org/10.1038/srep45678, 2017.

30 Taylor, J.: Introduction to error analysis, the study of uncertainties in physical measurements, 1997.

Tesche, M., Ansmann, A., Müller, D., Althausen, D., Engelmann, R., Freudenthaler, V., and Groß, S.: Vertically resolved separation of dust and smoke over Cape Verde using multiwavelength Raman and polarization lidars during Saharan Mineral Dust Experiment 2008, Journal of Geophysical Research: Atmospheres, 114, https://doi.org/10.1029/2009JD011862, 2009.

Tsekeri, A., Amiridis, V., Marenco, F., Nenes, A., Marinou, E., Solomos, S., Rosenberg, P., Trembath, J., Nott, G. J., Allan, J., et al.: Profiling
35 aerosol optical, microphysical and hygroscopic properties in ambient conditions by combining in situ and remote sensing, Atmospheric Measurement Techniques, 10, 83, https://doi.org/10.5194/amt-10-83-2017, 2017.

Weinzierl, B., Sauer, D., Esselborn, M., Petzold, A., Veira, A., Rose, M., Mund, S., Wirth, M., Ansmann, A., Tesche, M., et al.: Microphysical and optical properties of dust and tropical biomass burning aerosol layers in the Cape Verde region—an overview of the airborne in situ and lidar measurements during SAMUM-2, Tellus B, 63, 589–618, https://doi.org/10.1111/j.1600-0889.2011.00566.x, 2011.

Whiteman, D., Melfi, S., and Ferrare, R.: Raman lidar system for the measurement of water vapor and aerosols in the Earth?s atmosphere, Applied Optics, 31, 3068–3082, https://doi.org/10.1364/AO.31.003068, 1992.

Figure 1. Map of Cyprus showing the locations of the observation sites used for the measurements reported in this paper. The inset in the upper-left corner shows the greater area of South Europe, North Africa, and the Middle East, with the white square indicating the location of Cyprus. The maps were generated by Google Earth Pro (https://www.google.com/earth/download/gep/agree.html).

Figure 2. Photograph of the UAV of the Cyprus Institute used for the measurements reported in this work.
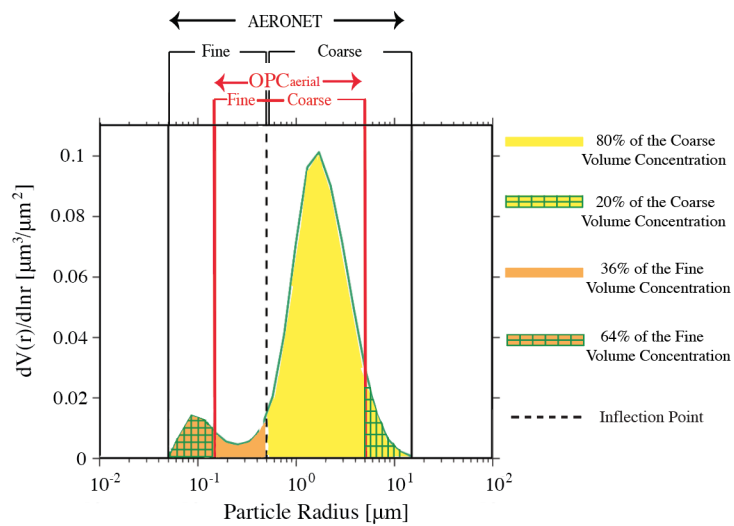
Figure 3. Column-integrated volume size distribution measured with the sunphotometer over Nicosia at 06:57 UTC on 15 April 2016. The ranges of particle sizes measured by AERONET sunphotometers, and by the OPC$_a$ are also indicated in the figure.
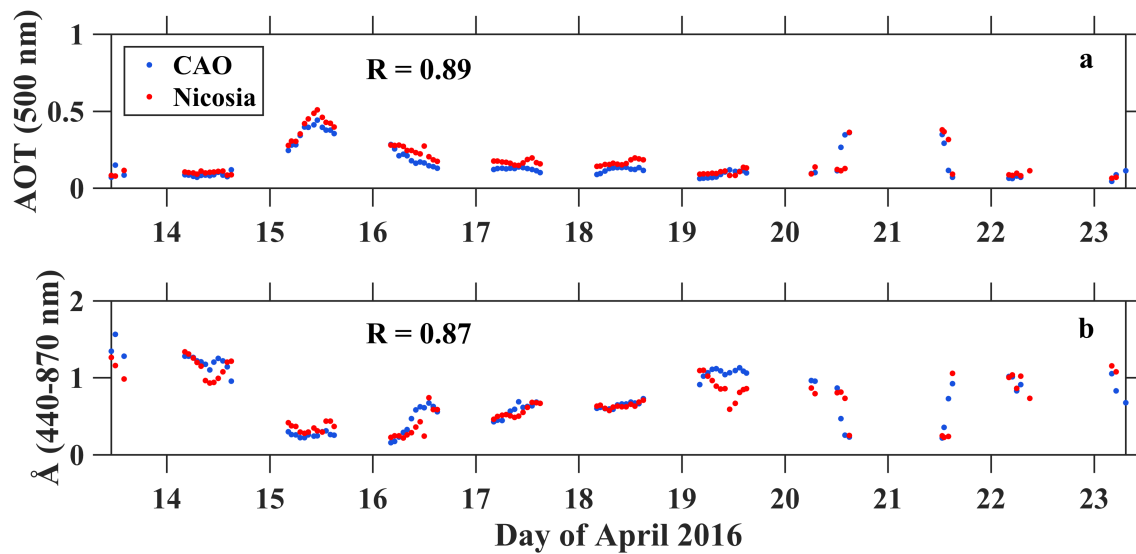
Figure 4. (a) AOT_{500} and (b) $Å_{440-870}$ as measured with the sun-photometers at CAO (blue circles) and Nicosia (red circles) from 13 to 24 April 2016.
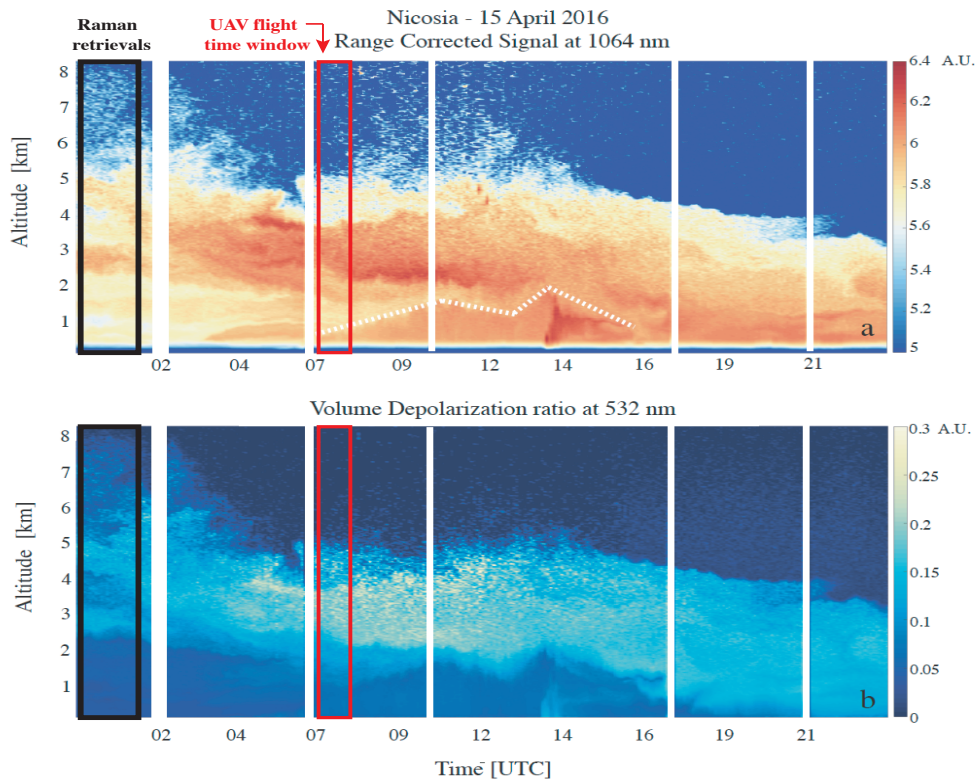
Figure 5. Range-corrected LIDAR signal at 1064 nm (a) and Volume Linear Depolarization ratio (b) reflecting the atmospheric conditions over Nicosia on 15 April 2016. Blue color indicates weak backscattering, yellow-red colors in the range corrected LIDAR signal (a) indicate backscattering mainly from fine aerosols and dust, whereas the dotted line shows the PBL top. The LIDAR observations used for the comparison with the UAV measurements were those recorded between 07:00-07:50 UTC.
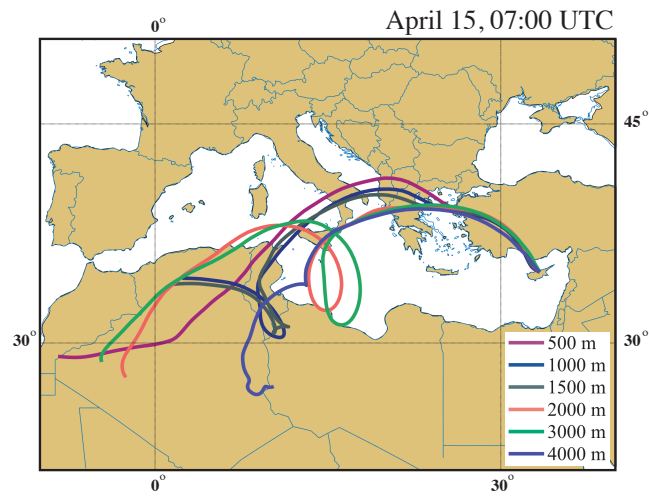
Figure 6. Back-trajectories of the air masses arriving at several altitudes over Cyprus on April 15, 07:00 (UTC). The back-trajectories were calculated for a duration of 5 days using the HYSPLIT transport and dispersion model (Rolph, 2003; Stein et al., 2015) with GDAS 1° meteorological data through the Real-time Environmental Applications and Display sYstem (READY; http://ready.arl.noaa.gov/index.php).
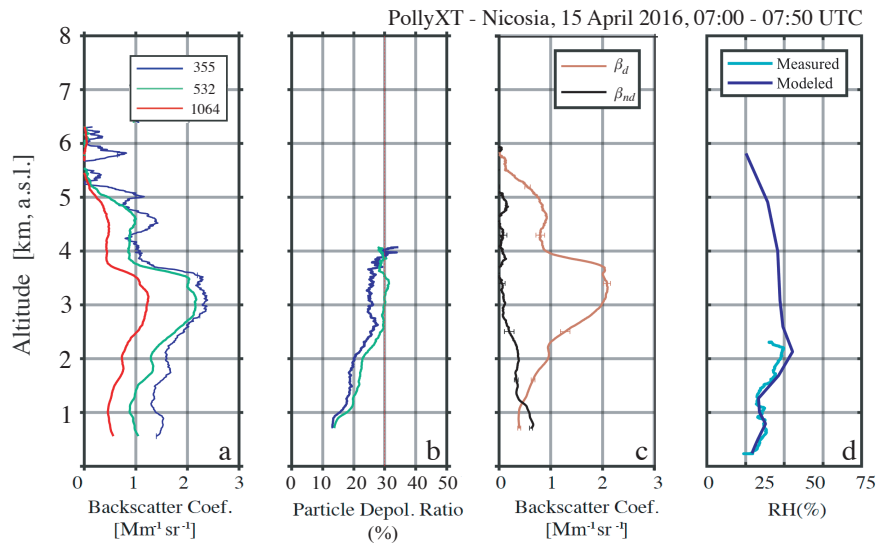
Figure 7. Day-time profiles of β (355-, 532-, and 1064-nm wavelength) (a) δ^p (355- and 532-nm wavelength) (b) β_d and β_{nd} (c) determined by POLIPHON, as well as RH profiles from in-situ measurements onboard the UAV and from WRF−ARW model simulations over Nicosia at 08:00 UTC (d).
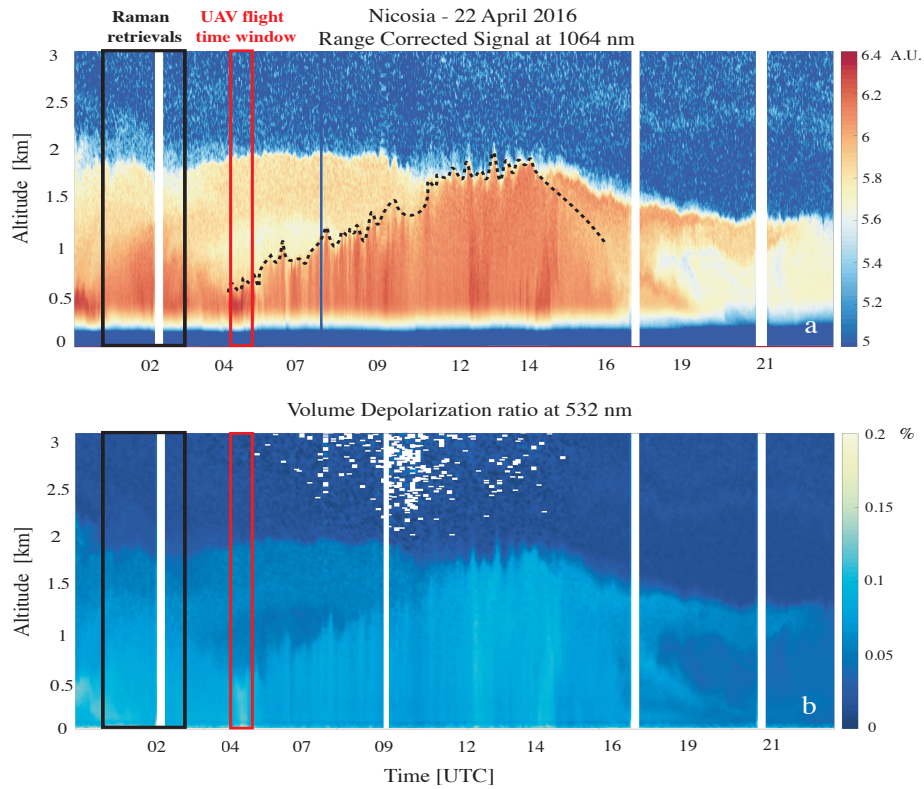
Figure 8. Range-corrected LIDAR signal at 1064 nm (a) and Volume Linear Depolarization ratio (b) reflecting the atmospheric conditions over Nicosia on 22 April 2016. Blue color indicates weak backscattering, yellow-red colors in the range corrected LIDAR signal (a) indicate backscattering mainly from fine aerosols and dust, whereas the dotted line shows the PBL top. The LIDAR observations used for the comparison with the UAV measurements were those recorded between 04:22-05:00 UTC.
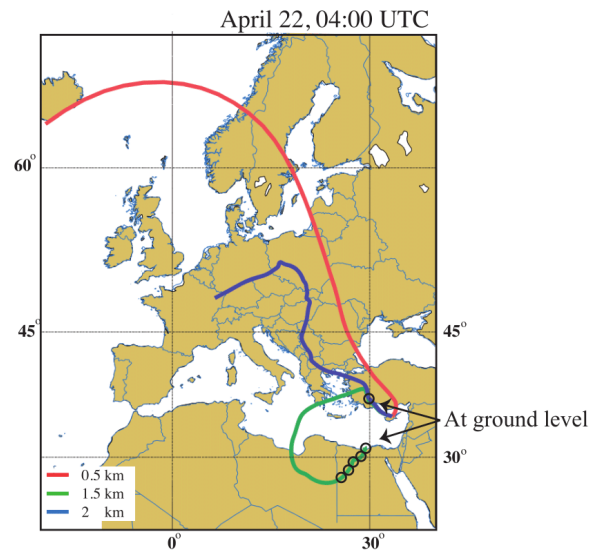
Figure 9. Back-trajectories of the air masses arriving at 500 m, 1000 m and 1500 m over Cyprus at 04:00 UTC on April 22. The back-trajectories were calculated for a duration of 6 days; the black circles indicate the locations where the air-mass was below 100 m altitude.
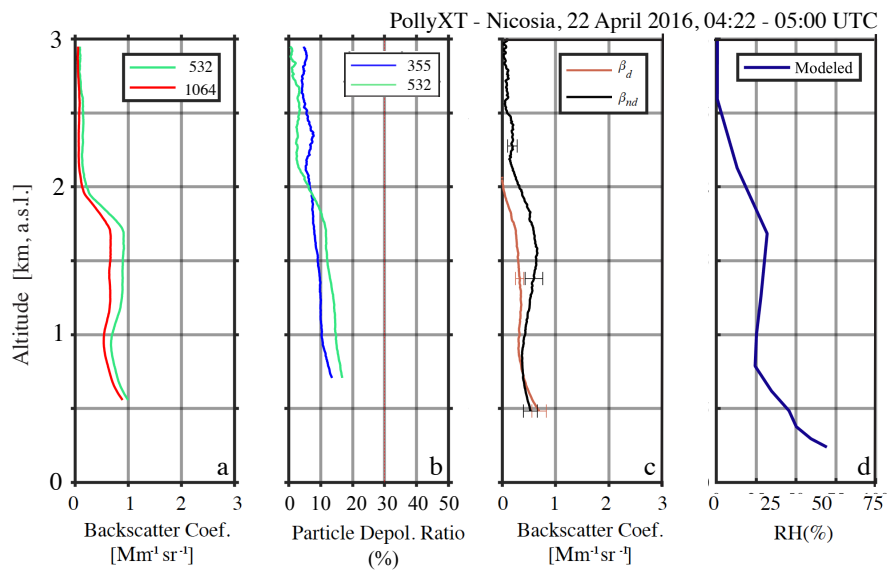
Figure 10. Day-time profiles of β (532-, and 1064-nm wavelength) (a) δ^p (355- and 532-nm wavelength) (b) β_d and β_{nd} (c) determined by POLIPHON, as well as RH profiles from WRF−ARW model over Nicosia at 04:00 UTC (d). The 355 nm channel of the LIDAR was discarded due to misalignment.
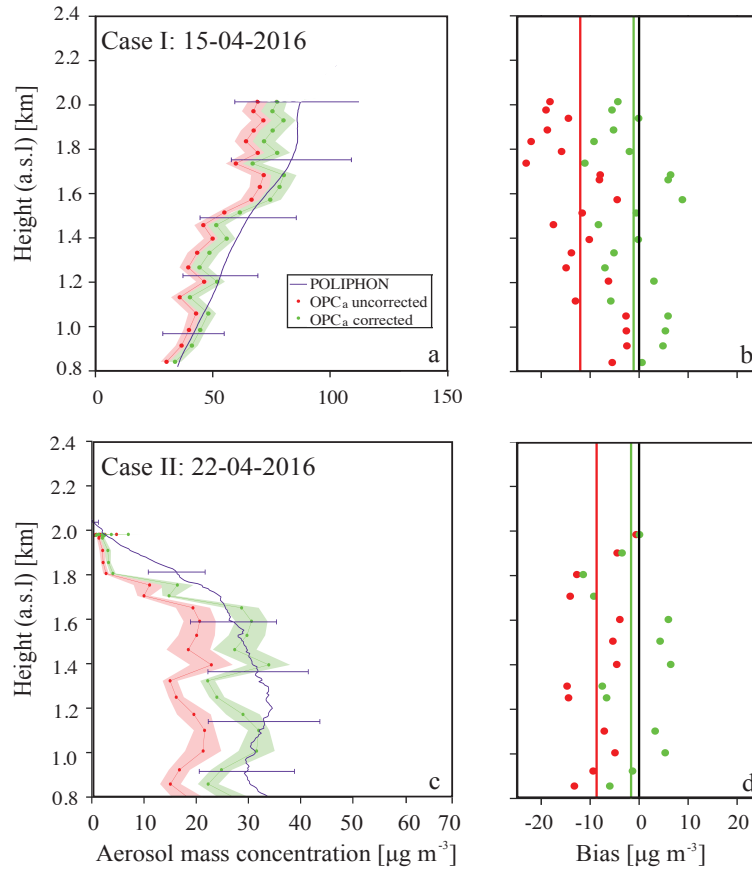
Figure 11. Aerosol mass concentration profiles for case study I and II (a, c) and the respective biases (b, d). In plots (a) and (c), the blue solid lines represent the mass concentration derived by the POLIPHON. The mass concentration measured by the OPC_a is plotted in red with the red shaded area representing the uncertainties of the in-situ measurement. The green lines show the mass concentration from the OPC_a corrected for the particles losses. In plots (b) and (d), the red dots show the biases between the values measured by the OPC_a and the LIDAR (OPC_a − LIDAR) before applying the corrections, while the green dots are the biases after corrections. The red and green solid lines show the mean biases before and after correction, respectively.

Table 1. Values of the input parameters used in the POLIPHON algorithm.

Parameter	Symbol	Values	Source/Reference
Dust depolarization ratio	δ_d	$31 \pm 4\%$	(Freudenthaler et al., 2009)
Non-dust depolarization ratio	δ_{nd}	$5 \pm 1\%$	(Ansmann et al., 2011)
Dust LIDAR ratio	S_d	47 ± 10 sr	Raman measurements, this study
Non-dust LIDAR ratio	S_{nd}	60 ± 10 sr	(Mamouri and Ansmann, 2014)
Dust particle density	ρ_d	$2.6 \pm 0.6\ g\ cm^{-3}$	(Hess et al., 1998)
Dust conversion factor (15.04.2016)	$\overline{v_c/\tau_c}$	$0.67 \pm 0.05 \times 10^{-6}$	Sunphotometer, this study
Non-dust conversion factor (15.04.2016)	$\overline{v_f/\tau_f}$	$0.24 \pm 0.018 \times 10^{-6}$	Sunphotometer, this study
Dust conversion factor (22.04.2016)	$\overline{v_c/\tau_c}$	$0.81 \pm 0.04 \times 10^{-6}$	Sunphotometer, this study
Non-dust conversion factor (22.04.2016)	$\overline{v_f/\tau_f}$	$0.14 \pm 0.019 \times 10^{-6}$	Sunphotometer, this study